Copper photodeposition on TiO2 studied with HREM and EXAFS

Copper Photodeposition on TiO_2 Studied with HREM and EXAFS

J. W. M. Jacobs

Philips Research Laboratories, 5600 JA Eindhoven, The Netherlands

F. W. H. Kampers

Laboratory for Inorganic Chemistry and Catalysis, Eindhoven University of Technology, 5600 MB Eindhoven, The Netherlands

J. M. G. Rikken and C. W. T. Bulle-Lieuwma

Philips Research Laboratories, 5600 JA Eindhoven, The Netherlands

D. C. Koningsberger

Laboratory for Inorganic Chemistry and Catalysis, Eindhoven University of Technology, 5600 MB Eindhoven, The Netherlands

ABSTRACT

The possibility of direct selective surface activation by photodeposition of autocatalytic Cu particles on photosensitive TiO_2 substrates in an alkaline electroless copper solution has been investigated. The nucleation and growth of particles were characterized by transmission electron microscopy (TEM). *Ex situ* high resolution TEM and *in situ* extended x-ray absorption fine structure (EXAFS) spectroscopy were used to determine the oxidation state of photodeposited particles on thin polycrystalline TiO_2 films and suspended TiO_2 powders, respectively. It is shown that in the initial stages of photodeposition small (<3 nm) noncatalytic Cu_2O particles are formed. Electroactive Cu particles are only observed at relatively long illumination times and/or high light intensities. These results are explained with a model of the illuminated TiO_2 crystallite/electrolyte interface, which considers simple redox reactions involving transfer of TiO_2 photoelectrons to energy levels of the couples between complexed Cu^{2+} ions, Cu_2O and Cu. From this it is concluded that under illumination Cu particles are only formed if deposition of Cu_2O is limited by either mass transport of complexed Cu^{2+} ions or kinetic factors.

In the last few years patterned electroless metal deposition has gained increasing attention for potential application in the fabrication of microelectronic devices (1-5). Basically, electroless metal deposition involves a heterogeneous catalytic electron-transfer reaction, in which electrons are transferred from a reducing agent to metal ions. It can be carried out selectively on patterned electroactive areas on the substrate, since deposition is autocatalytic and requires an electrocatalytic surface to start. In most cases, the active areas are obtained by the application of electrocatalytic metal nuclei on the substrate, for example by photoselective activation procedures (6, 7). A disadvantage of this procedure is that metallization involves at least two steps: activation and electroless metal deposition. Furthermore, reducible species, *e.g.*, adsorbed Pd ions, may be left behind at undesirable places on the substrate after the activation step. When these are reduced to electrocatalytic species in the electroless solution, the latter may cause uncontrolled, nonselective electroless metal deposition. Therefore, it seemed worthwhile to study the possibility of direct selective surface activation in an electroless solution.

In the work described in this paper, which is a continuation of earlier reports on different aspects of the initiation of electroless metal deposition (8-10), direct laser-induced copper deposition from an electroless copper solution on TiO_2 substrates is investigated. It was expected that photochemically deposited metallic Cu nuclei from an electroless solution on photosensitive TiO_2 films would show autocatalytic behavior. This means that prenucleated areas on the TiO_2 film should be intensified by subsequent electroless copper deposition in the dark. Preliminary experiments, however, showed that this only occurred after relatively long illumination times. This raised the question whether metallic Cu nuclei were photodeposited in the initial stages of illumination. Therefore our primary goal was to determine the oxidation state of the photodeposited copper species.

Although photoassisted deposition of copper species on TiO_2 single crystal electrodes (11, 12) and TiO_2 powders (12-15) has been previously observed, no efforts were made to determine the oxidation state of the deposited copper species. Hermann *et al.* suggested that Cu^{2+} ions in a TiO_2 suspension were photoreduced to Cu^+ ions and that metallic copper could not be obtained even by using acetic acid in the solution as a hole scavenger or by performing the photoreaction under reducing atmosphere (hydrogen) (14).

In this study, the nucleation densities and the sizes of photodeposited particles on TiO_2 films and powders were determined by transmission electron microscopy (TEM). A recently developed specimen preparation technique for thin polycrystalline TiO_2 films (16) was used to obtain high resolution electron microscopy (HREM) structure images of photodeposited particles. Complementary to these *ex situ* measurements, *in situ* extended x-ray absorption fine structure (EXAFS) measurements of photodeposited particles on suspended TiO_2 powders were performed by using a thin-layer fluid cell. It will be shown that photodeposition of Cu particles on TiO_2 is preceded by photodeposition of Cu_2O particles, which show only slight electrocatalytic activity in an electroless copper solution.

Experimental

Materials.—The aqueous electroless copper solution consisted of: (*i*) 0.04*M* $CuSO_4 \cdot 5H_2O$; (*ii*) 0.18*M* $KNaC_4H_4O_6 \cdot 4H_2O$ (potassium sodium tartrate); (*iii*) 0.25*M* NaOH, and (*iv*) 0.33*M* HCHO (17). Tartrate (Tart) is a complexing agent for Cu^{2+} ions and HCHO is the reducing agent active in electroless deposition. Two other solutions, from which HCHO or $CuSO_4$ and HCHO were omitted, are denoted by (Cu^{2+}, Tart, OH^-) and (Tart, OH^-), respectively. Experiments in which EDTA instead of tartrate was used as a complexing agent for Cu^{2+} ions gave similar results and are not reported here. All solutions were prepared from triply distilled water and all experiments were carried out at room temperature.[1]

Details of the preparation of TiO_2 films for HREM have been described elsewhere (16). Briefly, the HREM specimens consist of a thin (thickness <10 nm) polycrystalline TiO_2 (anatase) film on an amorphous Si_3N_4 membrane (size 15 × 15 μm^2; thickness 13 nm) supported by a small section of a Si(100) wafer. The TiO_2 film consists of a single

[1] Unless otherwise stated, nitrogen gas was not bubbled through the solution.

layer of 10-25 nm anatase crystallites. The TiO_2 powder which was used for EXAFS measurements was Eurotitania-1 (Tioxide batch no. 1143) consisting of 99% anatase with a surface area of about 46 m^2/g. EXAFS scans of Cu foil (Goodfellow Metals), Cu_2O powder (Merck), and CuO powder (Merck) were taken for comparison purposes and to obtain phase shift and backscattering amplitude functions for different absorber-scatterer pairs. The reference compound samples of Cu_2O and CuO had to be diluted with boron nitride to obtain an amount that could be pressed in a sample holder to form a self-supporting wafer with an x-ray absorbance of 2.5. The Cu_2O powder was checked with x-ray powder diffraction to be 99% pure Cu_2O. The Cu foil had an optical thickness of 8 μm and was 99.97% pure.

Illumination.—TiO_2 films.—The illumination of HREM specimens was carried out with a UV (Ar^+) laser beam (Spectra Physics 2025-05; wavelength 351.1-363.8 nm; beam diameter was 1.0 mm) which was focused onto the TiO_2 film by a long working-distance objective lens in a Leitz Orthoplan microscope. The laser spot with a diameter of 13 μm was centered at the edge of the Si_3N_4 window to facilitate comparison between illuminated and non-illuminated areas on the TiO_2 films (see Fig. 1). A quartz cell with an optical window thickness of 1.0 mm and a solution layer thickness of 2.0 mm was placed horizontally on the specimen table of the microscope. Illumination was started as soon as the specimen was placed in the quartz cell and imaged on a TV monitor. Light intensities (I) and illumination times (Δt) were varied between 1 and 10^3 W/cm^2 and between 1 ms and 10s, respectively.

Procedure f(A): After illumination in the electroless solution or the (Cu^{2+}, Tart, OH^-) solution, the specimen was immediately dipped in water for 15s and quickly dried in air.

Procedure f(B): After illumination in the (Cu^{2+}, Tart, OH^-) solution, the specimen was immediately transferred to the (Tart, OH^-) solution in which the previously irradiated spot was illuminated for a second time in order to reduce possibly deposited Cu^+ species to metallic copper. After that it was rinsed and dried as in procedure f(A).

TiO_2 powder.—200 mg TiO_2 powder was dispersed in 25 cm^3 of the (Cu^{2+}, Tart, OH^-) solution in a glass beaker. The electroless solution could not be used, since in that case spontaneous deposition of copper species was initiated in the dark. During illumination the suspension was agitated by a magnetic stirrer. The UV laser beam was expanded to a diameter of 15 mm and then directed into the beaker from above ($I \approx 100$ mW/cm^2). After each illumination the beaker was placed in a N_2 atmosphere and stirring was stopped. Most of the TiO_2 grains settled to the bottom of the beaker within 10 min.

Procedure p(A): After 20 min illumination and subsequent settling in the (Cu^{2+}, Tart, OH^-) solution, the sediment, *i.e.*, the TiO_2 grains with the surrounding (Cu^{2+}, Tart, OH^-) solution, was transferred into the EXAFS cell as described below [sample p(A)].

Procedure p(B): After 20 min illumination and subsequent settling in the (Cu^{2+}, Tart, OH^-) solution, 24 cm^3 of the supernatant solution was replaced by 24 cm^3 of the (Tart, OH^-) solution. After that, stirring was restarted and the TiO_2 suspension was illuminated again for 20 min. After settling, the sediment was transferred into the EXAFS cell [sample p(B)].

In order to correlate HREM data with EXAFS data, suspended TiO_2 grains were studied with TEM. A fraction of the sediment from procedure p(A) was washed thoroughly with water. Subsequently a copper grid, previously coated with a thin Formvar film, was dipped briefly in the TiO_2/water suspension and dried in air.

The time that elapsed between sample preparation and subsequent HREM or EXAFS measurements was less than 12h.

EXAFS fluid cell.—An assembly of a specially designed thin-layer fluid cell, used for EXAFS measurements of TiO_2 sediments, is shown in Fig. 2. The TiO_2 sediment was held between the two epoxy resin plates (b), which were reinforced with a carbon fiber fabric[2]. These windows have a low x-ray absorbance. A spacer (a) of the same material, with a recess in the shape of a funnel to accommodate the sample, was used to define the thickness of the sample. The thickness of the spacer (0.25 mm) was chosen to give approximately the optimum sample x-ray absorbance of 2.5 above the copper K-edge. The three plates were placed in two small polyethene envelopes (c) which were inserted into each other. The envelopes were placed between the rigid aluminum plates (d), which had the same shape as the spacer. Finally these were pressed tightly together by two other rigid U-shaped aluminum plates (e). The cell obtained in this way could be placed directly in the EXAFS spectrometer which is described below.

The EXAFS cell was filled in a N_2 filled glove bag in the following way. First, 10 mm^3 of the TiO_2 sediment was sucked up with a pipette and injected into the funnel of the spacer. The cell was then placed in a excicator which was evacuated three times, each time after admission of N_2 gas. In this way the sediment settled to the bottom of the funnel. This procedure was repeated five times. After filling, the tops of the polyethene envelopes were sealed to minimize penetration of air into the sediment. X-ray photography was used to verify that the cell was properly filled.

Electron microscopy investigations.—TEM and HREM investigations were carried out with a Philips EM400T

[2] Obtained from the Materials Development Group, Plastics Metalware Factories, Philips Eindhoven.

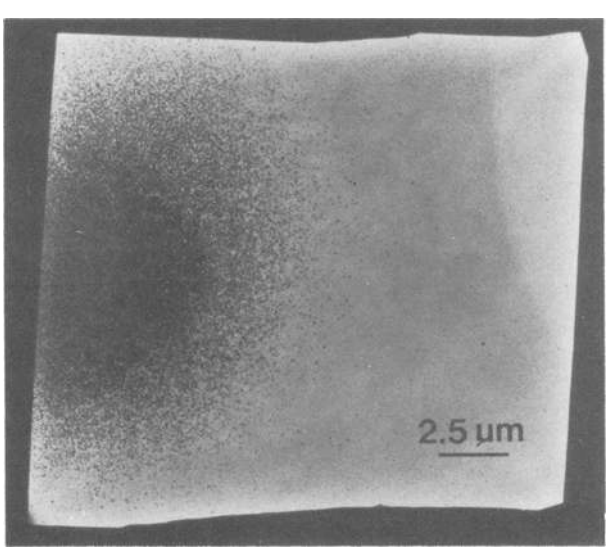

Fig. 1. Low-magnification TEM image of a spot photodeposited from the electroless solution and centered approximately on the left edge of the Si_3N_4/TiO_2 window. $\Delta t = 1s$; $I = 100$ W/cm^2.

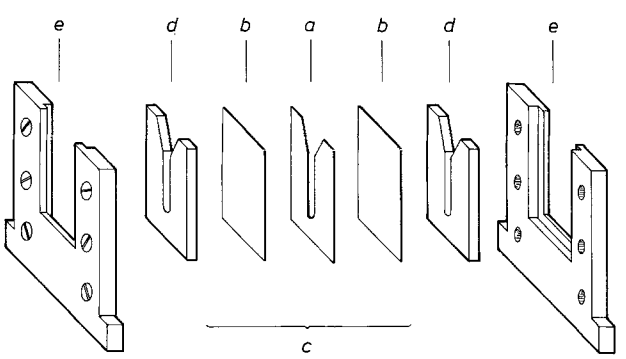

Fig. 2. Assembly of the EXAFS fluid cell. a: Spacer (thickness 0.25 mm) with funnel-shaped recess (size of the pipe of the funnel 5 × 27 × 0.25 mm^3), b: window plates (size 35 × 45 × 0.25 mm^3); c: polyethene envelopes (37 × 50 mm^2, foil thickness 25 μm); d: aluminum plates (35 × 45 × 4 mm^3); e: U-shaped aluminum plates.

(operated at 120 kV) and a Philips EM430ST (operated at 300 kV) transmission electron microscope, respectively. The technique of optical diffraction was used to analyze two-dimensional lattice images of a large number of photodeposited particles on HREM specimens. The measured (101) lattice spacing of 0.352 nm in anatase monocrystallites (18) provided a direct calibration of image magnification. Further details have been described elsewhere (9).

EXAFS investigations.—The EXAFS measurements were taken on a laboratory EXAFS spectrometer based on the Rowland circle principle (19-21). The radius employed was 500 mm. A Si (111) crystal with a diameter of 70 mm and modified Johansson geometry was used. The crystal is spherically bent over a radius of 1000 mm and spherically ground to the radius of the Rowland circle. A lead-clad slit system in front of the crystal was used to define the irradiated area of the crystal. This was chosen to be 10 mm high and 20 mm wide. The resolution at the copper K-edge was 17 eV.

An Elliot GX-21 rotating molybdenum anode x-ray generator was used, which was operated at a current of 200 mA and a tube voltage of 17 kV. The tube voltage was deliberately chosen below the molybdenum Kα excitation lines to prevent distortion of the spectra at half the energy of these lines. The structure factor for the (222) reflection in a perfect Si crystal equals zero. Bending the crystal will cause a deformation of the cubic lattice and a non-zero intensity for the radiation with twice the energy of the fundamental reflection.

A feedback loop acting on the tube current was used to stabilize the intensity of the monochromatic radiation when scanning through the $L\beta_1$ impurity line of tungsten at 9672.35 eV. However, this did not prevent distortions appearing in the spectra at that energy. For this reason the spectra were not used beyond 9650 eV.

At the focal point of the spectrometer a fixed 0.1×12 mm^2 tantalum slit prevented scattered radiation from entering the detector stage. A partially transparent ionization chamber monitored the incoming flux. The chamber was flushed with a 30% argon and 70% nitrogen mixture to give about 25% x-ray absorption at the copper K-edge. The transmitted intensity was measured with a totally absorbing Ar gasflow 2nd ionization chamber. Typically a full EXAFS scan took 20h.

Results

TiO_2 films.—General remarks.—At illumination times of the order of 1s optically visible spots with a diameter of ≈13 μm were photodeposited on TiO_2 films in the electroless solution. The rate of photodeposition in the (Cu^{2+}, Tart, OH^-) solution was found to be *ca.* 100× smaller than in the electroless solution. In the (Cu^{2+}, Tart, OH^-) solution all photodeposited spots dissolved slowly when the TiO_2 film was left in the solution after the illumination. This dissolution can be explained by an electroless corrosion mechanism, the cathodic process being the reduction of dissolved oxygen and the anodic process being oxidation (and complexation) of the deposited copper species (10). In the electroless solution, however, spots were intensified by autocatalytic copper deposition immediately after photodeposition when the illumination time (Δt) was larger than a critical value (Δt^*). The value of Δt^* was between 0.1 and 4s and increased when the light intensity was decreased. The growth of an autocatalytic spot ceased, however, after a short time and the spot remained stable in the solution.

TEM.—Short (<10 ms) light pulses resulted in the deposition of particles in the 0.5-3.0 nm size range in the electroless solution or in the (Cu^{2+}, Tart, OH^-) solution. The density of deposited particles in the (Cu^{2+}, Tart, OH^-) solution (10^9-10^{11}/cm^2) was much lower than in the electroless solution (10^{10}-10^{12}/cm^2). The density decreased when the light intensity was decreased. No particles were observed in the absence of illumination or in the absence of a TiO_2 film on the Si_3N_4 membrane. As in the case of Pd photodeposition on TiO_2 films (8), it was observed that, after a certain nucleation time, no new particles appeared and photodeposition occurred only on existing growth centers. The nucleation time in the (Cu^{2+}, Tart, OH^-) solution (0.1-5s) was much longer than in the electroless solution (1-10 ms) and increased when the light intensity decreased.

Figure 3 shows successive stages of photodeposition from the electroless solution at Δt = 3, 20, 100, and 1000 ms, respectively [procedure f(A); four different specimens]. At the light intensity used in this experiment (800 W/cm^2), Δt^* was ≈100 ms. Figure 3a shows particles in the 1.0-3.0 nm size range with a density of $\approx 5 \cdot 10^{11}$/cm^2. From Fig. 3b and 3c it is seen that, during subsequent illumination, the size range is extended to 3-6 nm and 3-40 nm, respectively. At 1000 ms the particles merged into a polycrystalline Cu layer (Fig. 3d), as was indicated by an electron diffraction image of this film (not shown).

HREM.—The crystal structures of particles (>1.5 nm), photodeposited from the electroless solution during illumination times less than Δt^* [procedure f(A)], were determined by HREM. All initially formed particles (<3 nm) had a structure of bulk Cu_2O. Nearly all particles larger than 3 nm had the structure of either bulk Cu_2O or bulk Cu (18), depending mainly on the light intensity. Only a few particles exhibited lattice images that indicated a deviation from the structure of Cu, Cu_2O or other copper (sub)oxides, such as Cu_4O (22, 23). It should be noted that, although both Cu and Cu_2O have a cubic structure, a distinction between the two phases can easily be made since the size of the Cu_2O unit cell [$a_0(Cu_2O)$ = 0.4269 nm] is 18% larger than that of the Cu unit cell [a_0(Cu) = 0.3615 nm] (18).

Although we did not try to quantify the ratio between the amount of photodeposited Cu_2O and Cu, it was established that at low light intensities (<10 W/cm^2) nearly all particles were Cu_2O, whereas at higher light intensities progressively more Cu particles were formed. At a fixed light intensity the fraction of Cu particles increased with increasing illumination times. Cu particles were already observed at illumination times less than Δt^*. In contrast with this, nearly all particles photodeposited from the (Cu^{2+}, Tart, OH^-) solution were identified as Cu_2O; only a few Cu particles (>3 nm) were observed at the highest light intensities (≈10^3 W/cm^2). Figure 4 shows three two-dimensional lattice images of Cu_2O particles along the [011], [111], and [112] zone axes, respectively. The sizes of the particles are 2, 4, and 10 nm, respectively. With each particle the corresponding optical diffraction pattern (ODP) and a schematic representation of the ODP are shown. The measured lattice spacings [$d(hkl)$] and angles are also indicated. In cases were spacings of equivalent sets of {hkl} planes could be measured, the average $d(hkl)$ value is indicated. The relevant interplanar spacings, obtained from the x-ray powder diffraction file of Cu_2O are: $d(110)$ = 0.3020 nm; $d(111)$ = 0.2465 nm; and $d(200)$ = 0.2135 nm (18). As seen from Fig. 4, the measured lattice spacings do not differ by more than 3% from the x-ray diffraction data. The measured angles between lattice planes

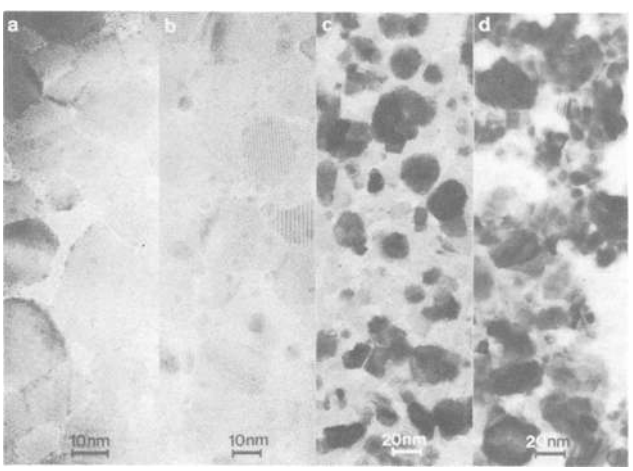

Fig. 3. TEM images of TiO_2-Si_3N_4 films showing successive stages of photodeposition from the electroless solution [procedure f(A)], I = 800 W/cm^2. a: Δt = 3 ms; b: Δt = 20 ms; c: Δt = 100 ms; d: Δt = 1000 ms.

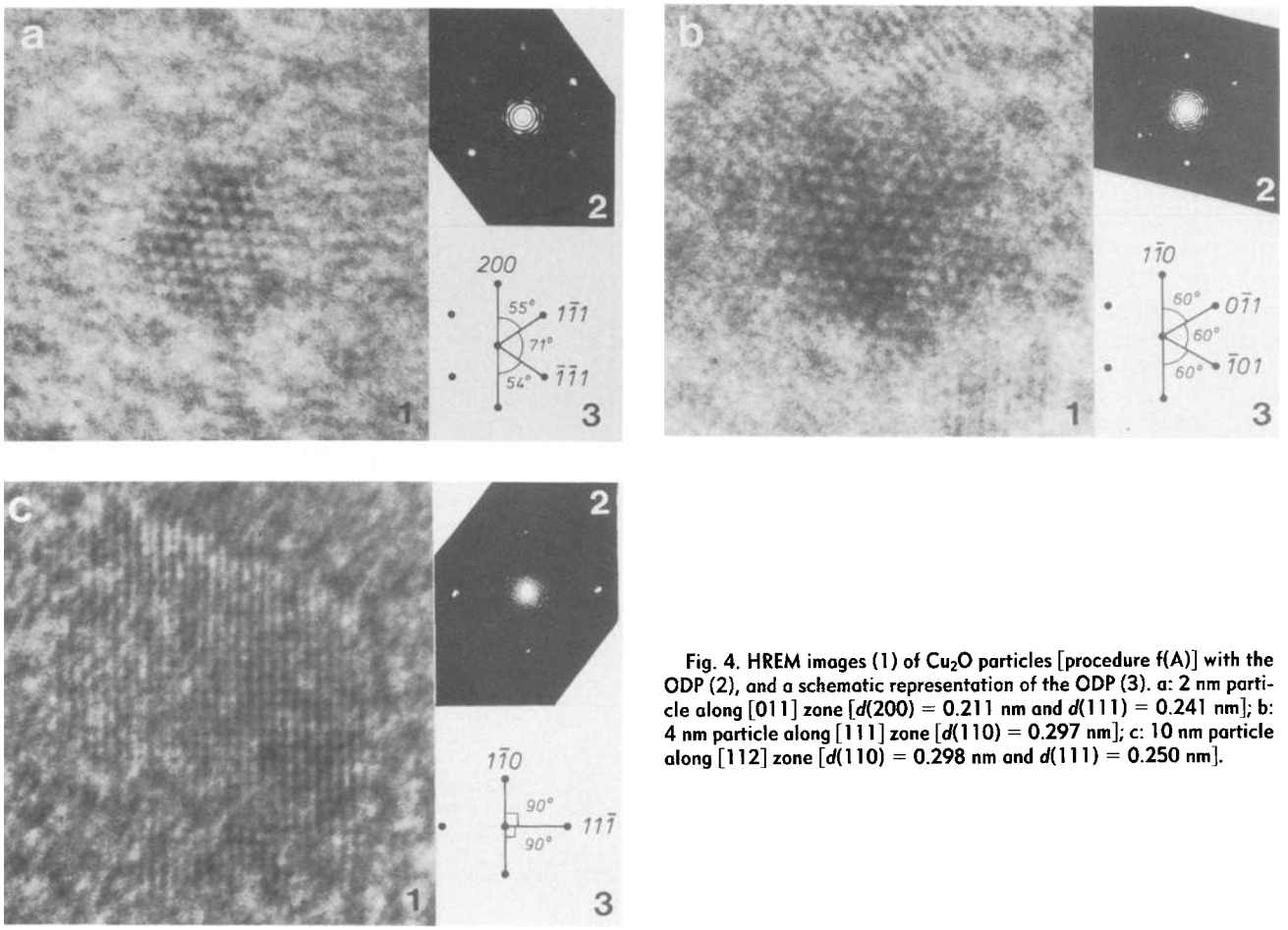

Fig. 4. HREM images (1) of Cu_2O particles [procedure f(A)] with the ODP (2), and a schematic representation of the ODP (3). a: 2 nm particle along [011] zone [d(200) = 0.211 nm and d(111) = 0.241 nm]; b: 4 nm particle along [111] zone [d(110) = 0.297 nm]; c: 10 nm particle along [112] zone [d(110) = 0.298 nm and d(111) = 0.250 nm].

also agree, within experimental error, with the values theoretically expected for a cubic structure. Single-crystalline and twinned Cu_2O particles as large as 25 nm were observed.

Figure 5 shows examples of [011] lattice images of three characteristic Cu particles with sizes of 7, 6, and 9 nm, respectively. The ODP of the single-crystalline Cu particle from Fig. 5a is similar to the ODP shown in Fig. 4a, except that the reciprocal distances are increased by ≈18%. A large number of Cu particles exhibited single or multiple twinning along the closely packed (111) planes. Examples of this are shown in Fig. 5b and 5c. The measured lattice spacings of the particles shown in Fig. 5 do not differ by more than 2% from the spacings reported for bulk Cu (18) [d(111) = 0.2088 nm and d(200) = 0.1808 nm].

The above observations show that Cu (Cu_2O) growth centers consist of well-defined crystallites. These probably grow by direct incorporation of reduced copper ions into the lattice. In contrast with this, it was found for Pd photodeposition that Pd growth centers consisted of a large number of randomly oriented 2-4 nm Pd clusters (8). In this case growth took place by repeated three-dimensional nucleation of 2-4 nm Pd clusters.

Finally, it was shown that all Cu_2O particles (>1.5 nm) that were photodeposited from the (Cu^{2+}, Tart, OH^-) solution were reduced to Cu particles when they were further illuminated in the (Tart, OH^-) solution for 2 min at 100 W/cm^2 [procedure f(B)]. Figure 6 shows [011] structure images of a 3 nm single-crystalline Cu particle (Fig. 6a) and a 3 nm single-twinned Cu particle (Fig. 6b), which were produced in this way. These results indicate that the atomic structure of photodeposited Cu_2O or Cu particles in procedure f(A) did not change during the sequence of rinsing with water, drying in air, exposure to air, transfer into the electron microscope and subsequent exposure to the electron beam.

TiO_2 powder.—General remarks.—Under illumination the color of the TiO_2 grains in the (Cu^{2+}, Tart, OH^-) solution gradually changed from white to pink within approximately 15 min [procedure p(A)]. However, the sediment obtained slowly regained its original white color when the solution remained in contact with air. This decolorization started at the top of the sediment, indicating dissolution of deposited copper species by the reduction of dissolved oxygen, which slowly diffuses into the sediment. During the second illumination in the (Tart, OH^-) solution the color of the TiO_2 grains gradually changed from pink to dark gray within approximately 10 min [procedure p(B)]. The color of the sediment slowly changed from dark gray via pink to white when the (Tart, OH^-) solution remained in contact with air. The dark gray color could not be obtained when the pink TiO_2 grains from procedure p(A) were thoroughly washed with a 0.25M NaOH solution and then illuminated in this solution. The color of naked TiO_2 powder in 0.25M NaOH also turned to blue-gray under illumination when dissolved oxygen was removed by N_2 bubbling or when hole scavengers, such as tartrate or HCHO, were added to this solution. This indicates the formation of reduced TiO_2 surface states (24).

When the TiO_2 sediment was stored in a N_2 atmosphere or in a sealed EXAFS cell immediately after the (final) illumination in procedure p(A) or p(B), the color of the TiO_2 grains did not change over several weeks. The TiO_2 sediment can then be considered as a "frozen" system without dissolved oxygen.

TEM.—Figure 7 shows a characteristic TEM image of TiO_2 powder obtained by illumination in the (Cu^{2+}, Tart, OH^-) solution for 20 min. It is seen that many particles in the 2-8 nm size range are randomly photodeposited on the TiO_2 crystallites which have a size in the 10-100 nm range. Multiple nucleation of small (1-3 nm) particles on one TiO_2 crystallite was also observed after a 5 min illumination. No deposits from the (Cu^{2+}, Tart, OH^-) solution were observed in the absence of either illumination or TiO_2 grains.

EXAFS data of samples and reference compounds.—Routine cubic spline background substraction and normalization methods were used to extract the EXAFS functions

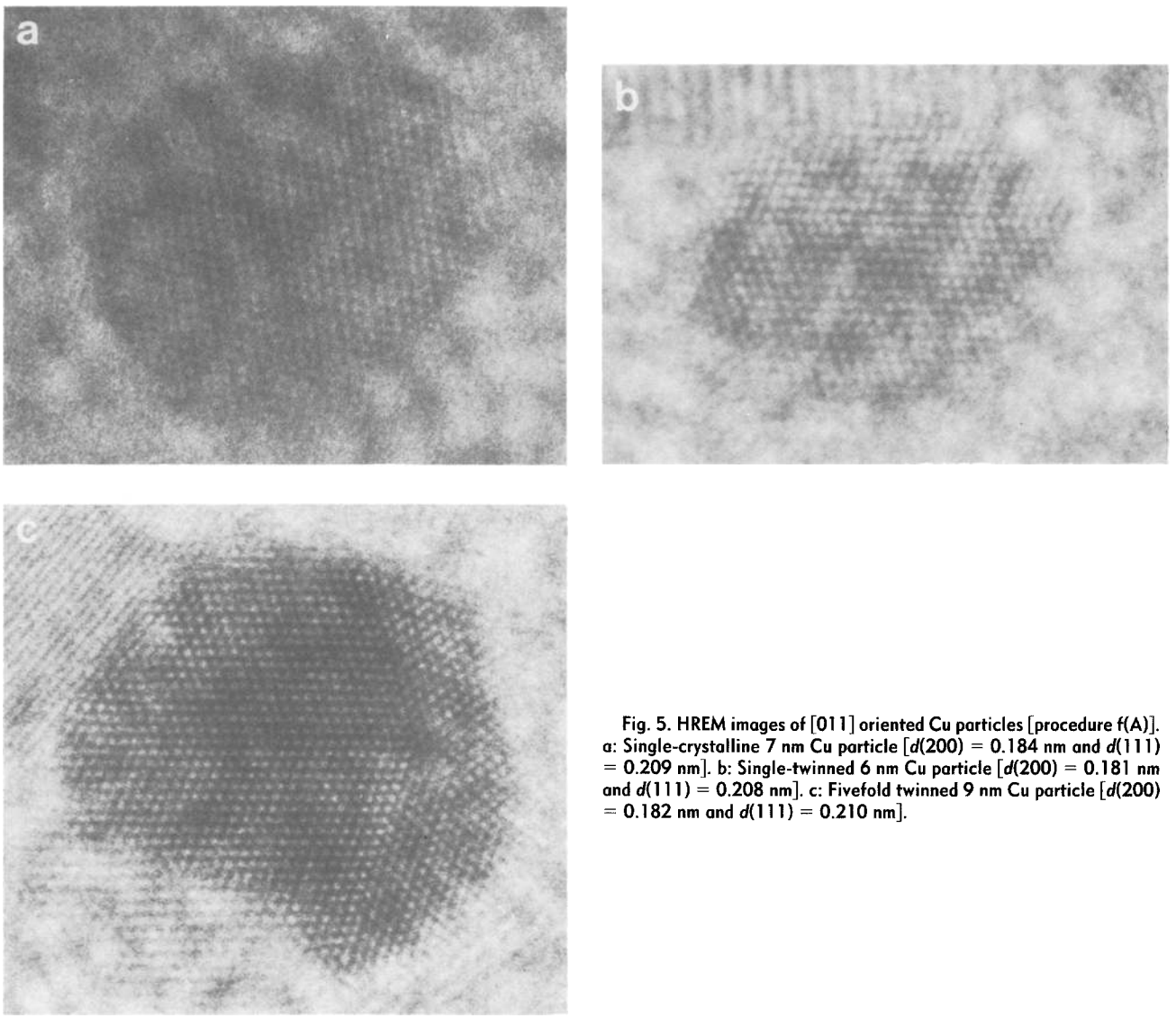

Fig. 5. HREM images of [011] oriented Cu particles [procedure f(A)]. a: Single-crystalline 7 nm Cu particle [$d(200) = 0.184$ nm and $d(111) = 0.209$ nm]. b: Single-twinned 6 nm Cu particle [$d(200) = 0.181$ nm and $d(111) = 0.208$ nm]. c: Fivefold twinned 9 nm Cu particle [$d(200) = 0.182$ nm and $d(111) = 0.210$ nm].

from the experimental data (25). The EXAFS spectra of the reference compounds and their k^3-weighted Fourier transforms are shown in Fig. 8. In Fig. 9 the spectra and k^3 Fourier transforms of the samples p(A) and p(B) are given. Because of the distortion of the spectra by the W impurity line the data could not be used beyond $k = 13$ Å^{-1}.

Fourier transforms of the EXAFS spectra are a first approximation of the radial distribution functions. Comparison of the Fourier transforms of the experimental data of sample p(A) with the CuO and Cu_2O reference data shows striking similarity between the sample and Cu_2O data (Fig. 10b). From the absolute mismatch in the imaginary part of the Fourier transforms of the sample and CuO data (Fig. 10a) it can be concluded that CuO is not the predominant copper phase. Furthermore the absence of a peak at the nearest neighbor distance (2.56 Å) in the fcc structure of Cu excludes the presence of a large amount of Cu in sample p(A).

If Fourier transforms of the data of sample p(B) are compared with the data of sample p(A) (Fig. 11a) and of Cu_2O (Fig. 11b) it can be concluded that the basis again is Cu_2O. However, an additional peak at the nearest neighbor distance of Cu is observed, which indicates the presence of metallic Cu.

EXAFS data analysis.—Quantification of the different contributions to the EXAFS signal requires a detailed analysis of the EXAFS data. The phase and backscattering amplitude functions for the different absorber-backscatterer pairs were obtained from the reference compound data (Table I) (25). These phase and backscattering amplitude functions, together with an estimate of the coordination number (N), the distance (R), the difference in the Debye-Waller factor between sample and reference compound ($\Delta\sigma^2$) and an inner potential correction (V_0), are used to calculate the EXAFS function of a particular coordination shell, expected to be present in the sample under study. The spectra of separate shells were added together to give the EXAFS of a model of the average local structure around a copper atom. Comparison in R space of both k^1 and k^3 Fourier transforms of the calculated and experimental data made it possible to find unique values for the seemingly correlated pairs N and $\Delta\sigma^2$ and R and V_0. The k range for the Fourier transformations was determined by the position of the nodes in the experimental data and was chosen as large as possible within the validity range of all references used.

The relatively poor energy resolution with which the spectra were measured does not affect the EXAFS function of all coordination shells in the same way (27). Because of the use of reference compounds, measured with the same resolution, absolute values of the coordination numbers and radii of equivalent coordination shells can still be obtained, but the values for low Z (oxygen) backscattering contributions in the spectra, especially at larger distances from the absorbing atom, have lower accuracy than for high Z (copper).

Figures 12 and 13 show the best results of the analysis in R space for sample p(A) and p(B), respectively. The coordination parameters used to calculate the models are listed in Tables II and III.

Discussion of EXAFS coordination parameters.—The results of the analysis of samples p(A) (Table II) indeed show

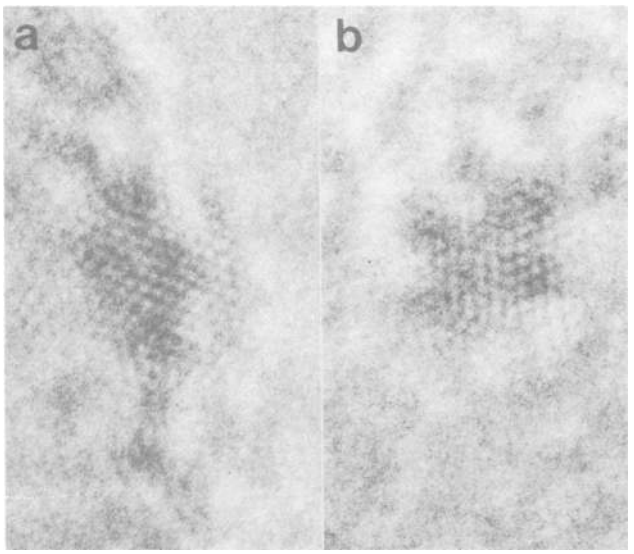

Fig. 6. HREM images of [011] oriented Cu particles [procedure f(B)]. a: Single-crystalline 3 nm Cu particle [$d(200) = 0.179$ nm and $d(111) = 0.206$ nm]. b: Single-twinned 3 nm particle [$d(200) = 0.182$ nm and $d(111) = 0.210$ nm].

great similarly with the parameters of Cu_2O powder. The coordination number and Cu^+-O^{2-} distance are, within the accuracy of the technique, equal to the values for bulk Cu_2O. The presence of a significant amount of copper suboxides (22, 23) can be excluded since the coordination number of the Cu^+-O^{2-} shell in these compounds is ≤ 1. The second largest peak is identified as the Cu^+-Cu^+ shell of the Cu_2O structure. In the sample the coordination number is smaller than the bulk value. The negative values of $\Delta\sigma^2$ indicate a smaller static disorder in the sample than in the reference compound.

In between these two shells there is a contribution which cannot be fitted with any of the absorber-scatterer combinations in Table I. It can be speculated that this contribution originates from a Cu-Ti substrate bond or from complexed copper ions in the solutions (28) but the quality of the data is insufficient to establish these hypotheses. Because of the overlap of the three shells in the Fourier transforms of the sample data it was necessary to approximate this contribution as effectively as possible by using the Cu^+-Cu^+ phase and backscattering amplitude functions, in order to be able to find reliable values for the parameters of the neighboring shells.

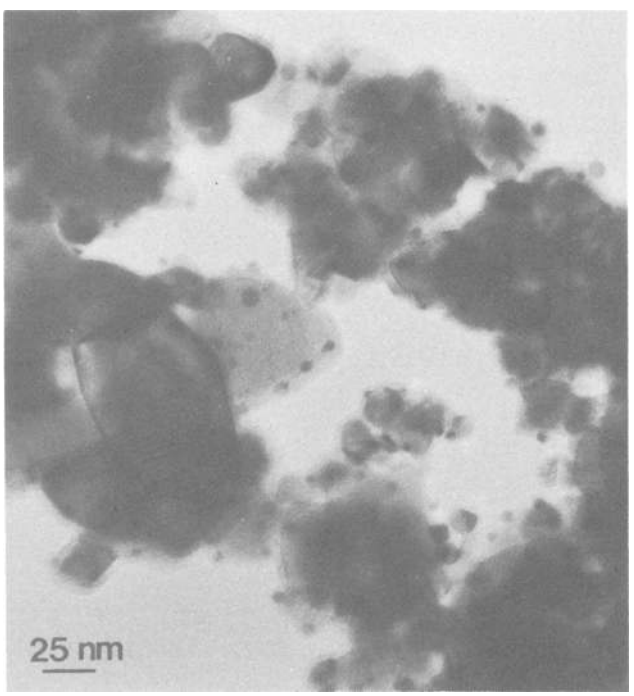

Fig. 7. TEM image of TiO_2 powder, which was illuminated in the (Cu^{2+}, Tart, OH^-) solution for 20 min [procedure p(A)]. Multiple nucleation of particles on TiO_2 crystallites is observed.

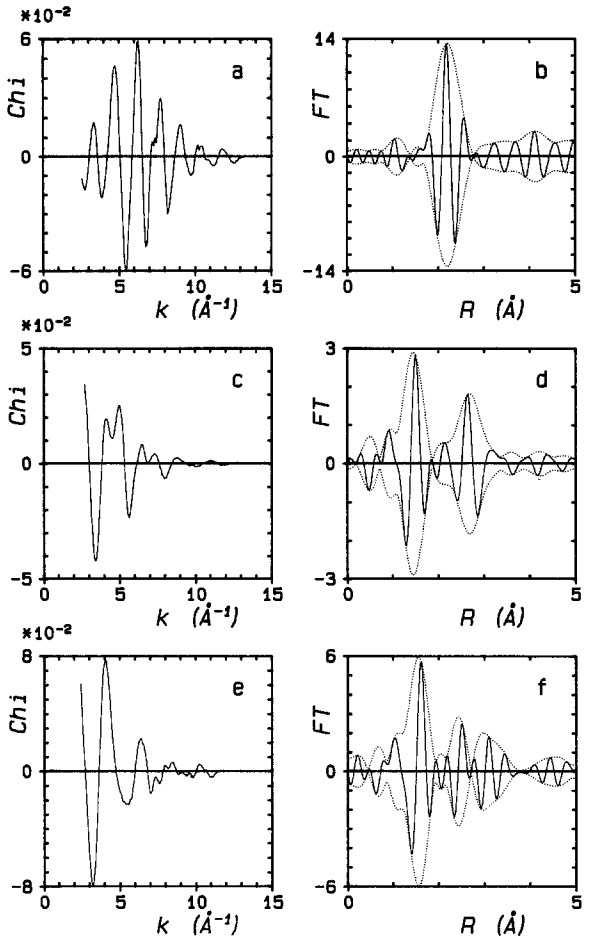

Fig. 8. EXAFS spectra of reference compounds and their k^3 weighted Fourier transforms (... absolute and ____ imaginary part). a: Spectrum of Cu foil, b: FT of a (k range 3.01-11.54 Å^{-1}). c: Cu_2O, d: FT of c (k range 2.98-11.44 Å^{-1}). e: CuO, f: FT of e (k range 2.72-11.49 Å^{-1}).

The first coordination shell in the data of sample p(B) again is identified as the Cu^+-O^{2-} shell in Cu_2O (Table III). The coordination number is equal to the bulk value for Cu_2O and is, within the accuracy of the technique, the same as for the first sample. The coordination distance is slightly larger than in the bulk. From the values of $\Delta\sigma^2$ for this shell it can be concluded that the static disorder in this shell is also larger than in the bulk.

The dominant peak in the Fourier transform of the data of sample p(B) originates from a combination of the Cu^0-Cu^0 shell in metallic Cu and the Cu^+-Cu^+ shell of Cu_2O. Compared to the value of 10 in the first sample, the coordination number of 0.8 for the Cu^+-Cu^+ shell is very low.

The fourth shell used to model the data cannot be attributed to either the Cu_2O or the Cu structure. Although necessary for reliable estimation of the coordination parameters of the other shells, no conclusions can be derived from the parameters of this shell.

Interpretation of EXAFS results.—Coordination numbers found with EXAFS are averages over all absorber element atoms. This affects EXAFS coordination numbers in two ways. In a sample that is a mixture of phases, the coordination number of a particular shell found from EXAFS analysis has to be corrected for the fraction of the total amount of absorber element atoms in the phase which incorporates that shell. Second, if the absorber element is present in particles, atoms near the surface of the particle will have incompletely filled coordination shells. There-

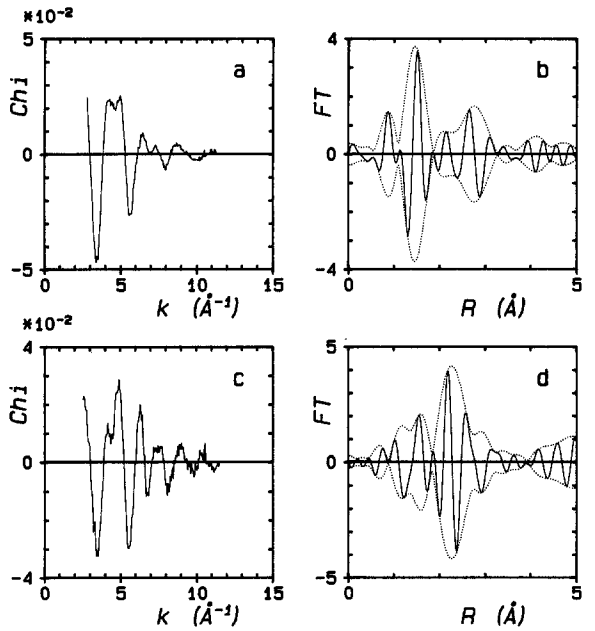

Fig. 9. EXAFS spectra of the samples together with their Fourier transforms (.... absolute part, ____ imaginary part). a: Spectrum of sample p(A), b: FT of a (k^3 weighted, k range 2.95-11.39 Å^{-1}). c: Sample p(B), d: FT of c (k^3, k range 3.02-11.53 Å^{-1}).

fore the average coordination number of a shell as found with EXAFS is a function of particle size (29). This effect will affect the coordination number of shells with larger radii more strongly.

The above analysis indicates that in sample p(A) almost all copper atoms are present in Cu_2O particles. From the coordination number of 10 for the Cu^+-Cu^+ shell it is estimated that the average Cu_2O particle size is 3-4 nm, assuming spherical particles. This agrees with TEM observations (cf. Fig. 7).

Since the coordination number found for the Cu^+-O^{2-} shell of sample p(B) equals the bulk value the fraction of copper atoms in the Cu_2O phase is approximately unity. Consequently the fraction of copper atoms in the Cu phase is very small. The coordination number of the Cu^0-Cu^0 shell has to be corrected for this fraction. This will result in a coordination number close to the bulk value (12), indicating relatively large Cu particles. The decrease of the coordination number of the Cu^+-Cu^+ shell from 10 in sample p(A) to 0.8 in sample p(B) indicates a considerable decrease in the Cu_2O particle size and/or a deviation from the spherical particle geometry. The fact that the coordination number of the Cu^+-O^{2-} shell is unaffected can be explained by the fact that this shell is relatively insensitive to particle size because saturation to the bulk value (2) occurs already in small particles (in one Cu_2O unit the coordination number already equals 1). Furthermore the dipole-dipole attraction between Cu_2O pairs can act as an additional force for completion of the Cu^+-O^{2-} shell of Cu_2O.

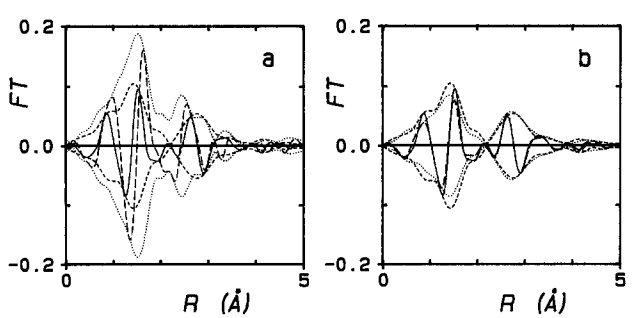

Fig. 10. Comparisons between k^1 weighted Fourier transforms of data of sample p(A) and those of CuO and Cu_2O (k ranges as in Fig. 9 and 10). a: Sample p(A) (---- absolute part, ____ imaginary part) and CuO (.... absolute part, — — imaginary part). b: Sample p(A) (---- absolute and ____ imaginary part) and Cu_2O (.... absolute part and — — imaginary part).

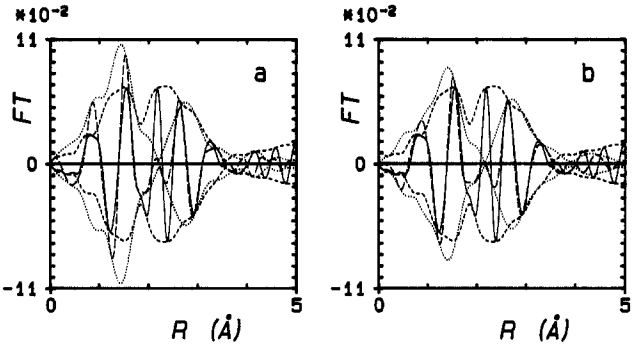

Fig. 11. Comparisons between k^1 weighted Fourier transforms of data of sample p(B) and those of sample p(A) and Cu_2O (k ranges as in Fig. 9 and 10). a: Sample p(B) (---- absolute part, ____ imaginary part) and sample p(A) (.... absolute part, — — imaginary part). b: Sample p(B) (---- absolute and ____ imaginary part) and Cu_2O (.... absolute part and — — imaginary part).

From the above analysis it is suggested that in sample p(B) all small particles consist of Cu_2O while larger particles consist of a Cu core, which might be covered with a few monolayers of Cu_2O. Apart from direct Cu_2O photodeposition a significant part of the Cu_2O may have been formed by the (partial) oxidation of previously formed Cu particles due to the presence of residual oxygen in the (Tart, OH^-) solution after the final illumination in procedure p(B). It should be noted that a thin (<0.5 nm) Cu_2O film, which might have been formed on previously formed Cu particles in procedures f(A) or f(B), cannot be observed by HREM.

Discussion

From the above results it is concluded that Cu_2O particles are photodeposited on TiO_2 crystallites in the presence of a relatively large amount of copper ions [procedures f(A) and p(A)]. Direct Cu photodeposition does not occur unless long illumination times and/or high light intensities are used. If the concentration of copper ions in the solution is decreased, Cu_2O particles can be reduced to Cu under illumination even at low light intensities. These results will now be discussed in terms of simple redox reactions involving transfer of TiO_2 photoelectrons to energy levels at the solid-liquid interface.

Energy diagram.—A simplified energy diagram of the TiO_2 crystallite—electrolyte interface at pH = 13.4, is shown in Fig. 14. All potentials are quoted *vs.* the normal hydrogen electrode (NHE). The following assumptions were used to construct this diagram.

The potentials of the valence bandedge and the conduction bandedge of TiO_2 are −0.85 and +2.15V, respectively (30). It is reasonable to assume that the energy bands in small TiO_2 crystallites (<100 nm) are flat, since an inter-

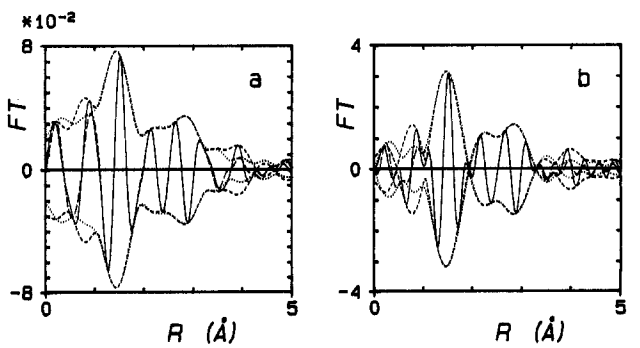

Fig. 12. Fourier transforms of experimental and calculated data for sample p(A). a: k^1 weighted, b: k^3 weighted, k range 3.84-10.69 Å^{-1}. (---- absolute part and ____ imaginary part of experimental data, ... absolute part and — — imaginary part of calculated data.)

Table I. Crystallographic data and particulars about the Fourier transforms on the reference compound data

Abs.-Scat. pair	N	R (Å)	Comp.	FT range ($Å^{-1}$)	k power	FT^{-1} range (Å)	Ref.
Cu^{+}-O^{2-}	2	1.85	Cu_2O	2.98-11.44	3	0 -1.88	(26)
Cu^{0}-Cu^{0}	12	2.56	Cu foil	3.01-13.22	3	1.48-2.94	(18)
Cu^{+}-Cu^{+}	12	3.02	Cu_2O	2.98-11.44	3	1.88-3.37	(26)

Table II. Results of analysis for sample p(A)

Shell	N	R (Å)	$\Delta\sigma^2$ ($Å^2$)	V_0 (eV)	Ref.
Cu^{+}-O^{2-}	2.1[a]	1.87[b]	−0.0025[a]	−1.6[a]	Cu^{+}-O^{2-}
?	0.3[c]	2.41[d]	−0.0190[c]	19[c]	Cu^{+}-Cu^{+}
Cu^{+}-Cu^{+}	10[a]	3.05[b]	−0.0017[a]	−2.2[a]	Cu^{+}-Cu^{+}

[a]Accuracy ±20%.
[b]Accuracy ±2%.
[c]Accuracy ±50%.
[d]Accuracy ±5%.

Table III. Results of analysis for sample p(B)

Shell	N	R (Å)	$\Delta\sigma^2$ ($Å^2$)	V_0 (eV)	Ref.
Cu^{+}-O^{2-}	2.0[a]	1.89[b]	0.0031[a]	−5.0[a]	Cu^{+}-O^{2-}
Cu^{0}-Cu^{0}	3.3[a]	2.60[b]	−0.0004[a]	−7.0[a]	Cu^{0}-Cu^{0}
Cu^{+}-Cu^{+}	0.8[c]	3.00[d]	0.0038[c]	6.0[c]	Cu^{+}-Cu^{+}
?	3.5[c]	3.37[d]	0.0030[c]	13[c]	Cu^{+}-O^{2-}

[a]Accuracy ±20%.
[b]Accuracy ±2%.
[c]Accuracy ±50%.
[d]Accuracy ±5%.

nal space charge layer, as present in bulk TiO_2 electrodes, cannot exist (8, 31, 32).

In the strongly alkaline electroless copper tartrate solution almost all copper ions are present as complexed ions [$(Cu^{2+})_c$]. The main uncomplexed copper ions are CuO_2^{2-} and $HCuO_2^{-}$, but their concentrations are orders of magnitude smaller than that of $(Cu^{2+})_c$ ions. Generally it is assumed that the reduction of copper ions occurs via $(Cu^{2+})_c$ ions (33-35).

$$(Cu^{2+})_c + 2e \rightarrow Cu \qquad [1]$$

El-Raghy and Abo-Salama measured the current-potential curve for this reaction at bulk Cu electrodes in the (Cu^{2+}, Tart, OH^{-}) solution (17). From an extrapolation of this curve to zero current one obtains the equilibrium potential −0.08V for reaction [1]. Assuming a reversible electron transfer, this potential corresponds approximately to the reversible redox potential for reaction [1] ($V((Cu^{2+})_c/Cu)$). The above value corresponds with polarographically determined values of $V((Cu^{2+})_c/Cu)$ for copper ions complexed by tartrate in alkaline medium (36).

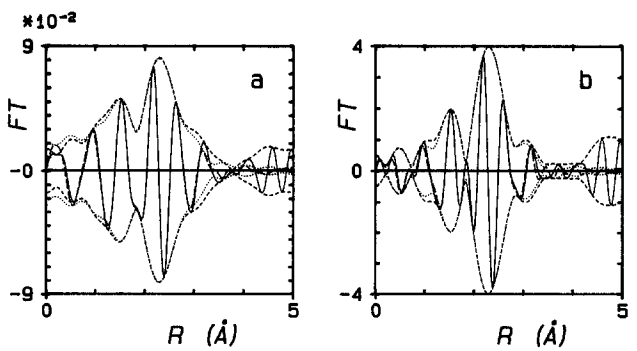

Fig. 13. Fourier transforms of experimental and calculated data for sample p(B). a: k^1 weighted, b: k^3 weighted, k range 3.91-10.73 $Å^{-1}$. (---- absolute part and ____ imaginary part of experimental data, ... absolute part and — — imaginary part of calculated data.)

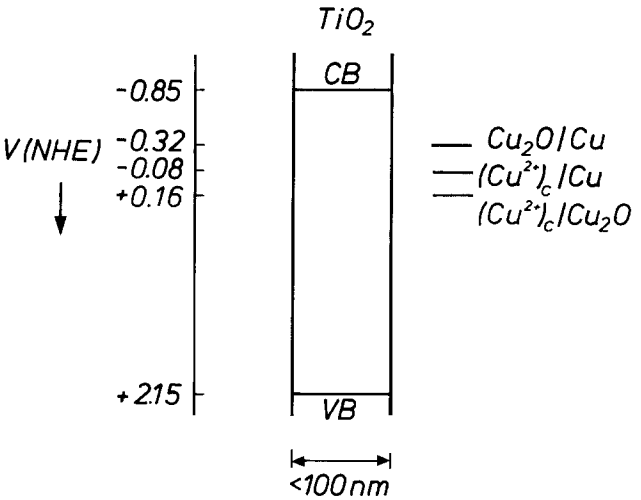

Fig. 14. Simplified energy diagram showing the conduction band (CB) and valence band (VB) edges of a TiO_2 crystallite at pH = 13.4 with respect to redox levels relevant to this work.

Cu_2O is electrochemically reduced to Cu according to

$$Cu_2O + H_2O + 2e \rightarrow 2Cu + 2\,OH \qquad [2]$$

From a thermodynamic point of view, this occurs at potentials more negative than the reversible redox potential $V(Cu_2O/Cu)$, which equals −0.32V at pH = 13.4 [37]. From numerous studies (38-40), however, it is known that reaction [2] may require significant overpotentials.

By subtracting reaction [2] from reaction [1] one obtains the reaction in which $(Cu^{2+})_c$ ions are reduced to Cu_2O

$$2(Cu^{2+})_c + 2\,OH^{-} + 2e \rightarrow Cu_2O + H_2O \qquad [3]$$

Using the above values of $V((Cu^{2+})_c/Cu)$ and $V(Cu_2O/Cu)$, it follows from a simple thermodynamic calculation that the reversible redox potential for reaction [3] ($V(Cu^{2+})_c/Cu_2O$) equals +0.16V.

Although Cu_2O films on Cu electrodes show the characteristics of a p-type semiconductor, the cathodic photocurrent in the presence of several redox systems is generally small and does not lead to self-reduction of Cu_2O to Cu (41). It was experimentally verified that photodeposition did not occur on suspended Cu_2O powder in the (Cu^{2+}, Tart, OH^{-}) solution. Therefore the photoelectrochemical contribution of Cu_2O particles to the formation of Cu can be neglected.

Photonucleation of Cu_2O.—In order to explain the initial photonucleation of small (<3 nm) Cu_2O particles on TiO_2 crystallites [procedures f(A) and p(A)], we consider the shift of the Fermi level[3] in the TiO_2 crystallites due to illumination. Since deposition of copper species from the (Cu^{2+}, Tart, OH^{-}) solution does not occur in the dark, it can be assumed that initially the Fermi level is below the onset potential for the reduction of $(Cu^{2+})_c$ ions (Fig. 14). Under illumination the photogenerated holes are rapidly transferred to oxidizable species in the solution (8). Both HCHO and tartrate are effective scavengers of the reactive valence band holes (42).

The photogenerated electrons may accumulate in the bulk of the crystallite but, most probably, they are trapped in surface states, as was indicated by recent memory effect experiments (8). The negative charging of the TiO_2 crystallites implies an upward shift of the Fermi level. The TiO_2 energy bandedges at the surface will also be shifted upward with respect to energy levels in the electrolyte, because the potential drop across the Helmholtz double layer will adjust itself to the extra negative charge on the TiO_2 crystallite (8).

[3] Strictly speaking the Fermi level concept only applies to situations in the dark in which equilibrium exists between electrons and holes. During illumination one can use the concept of quasi-Fermi levels for electrons and holes, respectively. Therefore the term "Fermi level" used in the text may refer to the quasi-Fermi level of electrons.

Possibly a number of photoelectrons will be used for the reduction of dissolved oxygen (43), but this will be disregarded. When a critical concentration of electrons is built up in the TiO_2 crystallite, *i.e.*, when the Fermi level has been shifted upward sufficiently, $(Cu^{2+})_c$ ions will be reduced. Since in alkaline medium the potential $V((Cu^{2+})_c/Cu_2O)$ is positive with respect to the potential $V((Cu^{2+})_c/Cu)$ (Fig. 14), it can be understood that the reduction of $(Cu^{2+})_c$ ions initially leads to the formation of small (<3 nm) Cu_2O particles according to reaction [3]. This agrees with the observation that relatively thick (≈5 μm) polycrystalline Cu_2O films were electrodeposited onto metal electrodes from an alkaline solution at small overpotentials (44, 45). Apparently, Cu_2O is able to conduct electrons rather well.

The observed multiple nucleation of Cu_2O particles on a TiO_2 crystallite (Fig. 3 and 7) and their growth can be explained by considering the modulation of energy bands inside the TiO_2 crystallite caused by the deposition of small (<3 nm) Cu_2O particles. The potential of the Cu_2O particles will initially be fixed near the redox potential of reaction [3]. The intrinsic barrier height at the TiO_2-Cu_2O contact determines whether the TiO_2 surface energy bandedges at the contact are shifted upward or downward with respect to those at naked sites (46, 47). A crucial point is that for one small (<3 nm) Cu_2O deposit the band modulation inside the TiO_2 crystallite decreases rapidly toward the interior of the crystallite (46-48). This implies that the energy levels in the larger part of the TiO_2 crystallite are not significantly affected by just one small Cu_2O deposit. Therefore multiple nucleation of small Cu_2O particles proceeds at other surface sites on the TiO_2 crystallites by the release of trapped photoelectrons.

After an initial nucleation period photodeposition only occurs on existing growth centers, as was observed for both TiO_2 films (Fig. 3) and suspended TiO_2 powder crystallites (Fig. 7). The reason for this is that photoelectrons are then sufficiently attracted to the Cu_2O deposits by a small electric field which has been build up inside the TiO_2 crystallites due to the presence of these deposits (48). The Cu_2O deposits serve as potential wells for photoelectrons (8).

Photodeposition of Cu_2O and Cu.—The formation of Cu_2O and/or Cu particles (>3 nm) during prolonged illumination [procedures f(A) and p(A)] depends strongly on the experimental conditions. It is assumed that during illumination the Fermi levels in the TiO_2 crystallite and the copper deposit are equal. When the rate of removal of photoholes from the TiO_2 crystallite is smaller than the maximum possible rate of transfer of photoelectrons through reaction [3], the Fermi level will be pinned near the redox potential of reaction [3] during illumination. This will only be true if the rate of reaction [3] is not limited by either mass transport of $(Cu^{2+})_c$ ions or kinetic factors. This explains the photodeposition of larger (>3 nm) Cu_2O particles, without significant formation of Cu, as observed in procedure p(A) and in procedure f(A) at relatively low light intensities. It can simply be calculated that in procedure p(A) the maximum spherical diffusion flux of $(Cu^{2+})_c$ ions to suspended TiO_2 crystallites is much larger than the flux of photons. In procedure f(A) the $(Cu^{2+})_c$ ions consumed at the illuminated spot on the TiO_2 film can be effectively replenished by three-dimensional diffusion of $(Cu^{2+})_c$ ions when the photon flux is not too large.

The Fermi level will rise beyond the redox potential of reaction [3] when the rate of negative charging of the TiO_2 crystallites due to illumination is larger than the rate of reaction [3]. When the Fermi level has risen above the potential $V((Cu^{2+})_c/Cu)$, $(Cu^{2+})_c$ are reduced directly to Cu according to reaction [1]. A rise of the Fermi level to a value sufficiently above the potential $V(Cu_2O/Cu)$ will result in the reduction of previously photodeposited Cu_2O particles to Cu particles according to reaction [2]. Both reactions [1] and [2] occurred during prolonged illumination in procedure f(A) at higher light intensities because the photoreduction of $(Cu^{2+})_c$ ions to Cu_2O became limited by mass transport. The occurrence of reaction [2] is most clearly illustrated by the results of procedures f(B) and p(B). During the second illumination of the system Cu_2O/TiO_2 in the (Tart, OH^-) solution, reactions [1] and [3] obviously could not occur while tartrate still acted as an effective hole scavenger.

Electroless copper deposition.—It can now be understood why photodeposited spots from the electroless solution on TiO_2 films only show autocatalytic behavior in the dark when the illumination time is longer than Δt^*.

As explained recently, electroless copper deposition on a small isolated spot can only be initiated and maintained when the current density of oxidation of the reducing agent HCHO at the spot (j(HCHO)) is greater than the current density of the reduction of dissolved oxygen at the spot ($j(O_2)$) (10). It is known that at bulk Cu electrodes the anodic oxidation of HCHO is a kinetically determined reaction (49), while the cathodic O_2 reduction reaction is controlled by mass transport at sufficiently negative potentials (50). Because Cu_2O shows a much lower electrocatalytic activity for the anodic oxidation of HCHO than Cu (49), j(HCHO) is roughly proportional to the total surface area of the photodeposited Cu particles. The maximum value of $j(O_2)$ is determined by a steady-state nonlinear diffusion flux of dissolved oxygen, which is inversely proportional to the spot diameter (10).

When Δt is smaller than Δt^* the larger fraction of the photodeposited particles in the spot consists of Cu_2O. Consequently j(HCHO) is too small to initiate electroless copper deposition (10). The surface area of active Cu particles is only large enough when Δt is larger than Δt^*. But even in this case it was observed that electroless copper deposition ceased after a short time. This inhibition effect is caused by the fact that $j(O_2)$ is larger than j(HCHO), due to an effectively enhanced supply of dissolved oxygen to the small spot by nonlinear diffusion (10). This implies that the initially active spot, formed by photodeposition, becomes passivated by oxidation of the copper surface.

This so-called oxygen-diffusion-size effect becomes less important when $j(O_2)$ becomes smaller, *i.e.*, when the photodeposited spot becomes larger than 13 μm or when the density of photodeposited copper patterns becomes higher. It was indeed observed that 36 copper spots (13 μm) deposited close together did show permanent autocatalytic behavior after photodeposition (10). Thus it may be expected that high-density electroless copper patterns with micron-sized structures can be deposited on TiO_2 films and other photosensitive substrates by direct photoselective surface activation (*e.g.*, by mask projection) in an electroless copper solution.

Conclusions

A detailed HREM and EXAFS investigation made it possible to characterize the process of photodeposition of copper species on TiO_2 substrates from an alkaline electroless copper solution. In the initial stages of UV illumination $(Cu^{2+})_c$ ions are photoreduced, leading to multiple nucleation of small (<3 nm) Cu_2O particles on TiO_2 crystallites. During prolonged illumination the existing Cu_2O particles grow and the nucleation rate decays to zero. Since Cu_2O shows only a low electrocatalytic activity for oxidation of HCHO, subsequent electroless copper deposition in the dark is not initiated. Electroactive Cu particles on TiO_2 films are only observed at relatively long illumination times and/or high light intensities. Previously photodeposited Cu_2O particles can be reduced to Cu particles during a second illumination in a solution from which $(Cu^{2+})_c$ ions are removed.

These observations are explained by the following model, which considers the rise of the Fermi level in the illuminated TiO_2 crystallites due to effective scavenging of photogenerated holes by reducing agents in the solutions. Photonucleation of Cu_2O particles starts when the Fermi level reaches the redox potential $V((Cu^{2+})_c/Cu_2O)$. Cu particles are not formed initially since in alkaline medium $V((Cu^{2+})_c/Cu_2O)$ is positive with respect to the redox potential $V((Cu^{2+})_c/Cu)$. As long as photodeposition of Cu_2O is not limited by either mass transport of $(Cu^{2+})_c$ ions or kinetic factors, the Fermi level is pinned near $V((Cu^{2+})_c/Cu_2O)$. However, when the rate of negative charging of the TiO_2 crystallites is larger than the rate of photodeposition

of Cu_2O, the Fermi level can reach the potential $V((Cu^{2+})_c/Cu)$, at which $(Cu^{2+})_c$ ions are reduced directly to Cu. Furthermore, a rise of the Fermi level to a value sufficiently above the potential $V(Cu_2O/Cu)$ will result in the reduction of previously photodeposited Cu_2O particles to Cu particles.

Finally, it is concluded that direct selective surface activation by photodeposition of autocatalytic copper particles on photosensitive TiO_2 substrates in an electroless copper solution is possible under conditions of mass transport limitation of $(Cu^{2+})_c$ ions. These can be achieved by relatively long illumination times, high light intensities and/or large surface areas of illuminated high-density patterns.

Acknowledgment

The authors thank Dr. D. Schryvers (University of Antwerp) for producing initial HREM images of photodeposited Cu_2O particles and Professor J. J. Kelly (State University of Utrecht) and J. E. A. M. van den Meerakker for very helpful discussions.

Manuscript submitted Aug. 18, 1988; revised manuscript received Jan. 3, 1989.

Philips Research Laboratories assisted in meeting the publication costs of this article.

REFERENCES

1. R. J. von Gutfeld, R. E. Acosta, and L. T. Romankiw, *IBM J. Res. Develop.*, **26,** 136 (1982).
2. Y. Harada, K. Fushimi, S. Madokoro, H. Sawai, and S. Ushio, *This Journal*, **133,** 2428 (1986).
3. A. Gemmler and J. L. Jostan, *Galvanotechnik*, **77,** 51 (1986).
4. C. H. Ting, Abstract 512, p. 720, The Electrochemical Society Extended Abstracts, Vol. 87-2, Honolulu, HI, Oct. 18-23, 1987; C. H. Ting, M. Paunovic, and G. Chiu, *ibid.*, Abstract 514, p. 723.
5. R. C. Sausa, A. Gupta, and J. R. White, *This Journal*, **134,** 2707 (1987).
6. M. Paunovic, *ibid.*, **127,** 441 (1980).
7. A. Gemmler, J. L. Jostan, and A. F. Bogenschutz, *Metalloberfläche*, **38,** 343, 388 (1984).
8. J. W. M. Jacobs, *J. Phys. Chem.*, **90,** 6507 (1986).
9. J. W. M. Jacobs, and D. Schryvers, *J. Catal.*, **103,** 436 (1987).
10. J. W. M. Jacobs and J. M. G. Rikken, *This Journal*, **135,** 2822 (1988).
11. M. S. Wrighton, P. T. Wolczanski, and A. B. Ellis, *J. Solid State Chem.*, **22,** 17 (1977).
12. H. Reiche, W. W. Dunn, and A. J. Bard, *J. Phys. Chem.*, **83,** 2248 (1979).
13. K.-H. Stadler and H. P. Boehm, "Proceedings of the 8th International Congress on Catalysis," Berlin (1984), Vol. IV, p. 803, Verlag Chemie, Weinheim (1984).
14. J.-M. Hermann, J. Disdier, and P. Pichat, *J. Phys. Chem.*, **90,** 6028 (1986).
15. R. Baba, R. Konda, A Fujishima, and K. Honda, *Chem. Lett.*, 1307 (1986).
16. J. W. M. Jacobs and J. F. C. M. Verhoeven, *J. Micros.*, **143,** 103 (1986).
17. S. M. El-Raghy and A. A. Abo-Salama, *This Journal*, **126,** 171 (1979).
18. TiO_2: ASTM file 21-1272; Cu: ASTM file 4-0836; Cu_2O: ASTM file 5-0667.
19. J. B. A. D. van Zon, Thesis, Eindhoven University of Technology (1984).
20. P. Brinkgreve, T. M. J. Maas, D. C. Koningsberger, J. B. A. D. van Zon, M. H. C. Janssen, A. C. M. E. van Kalmthout, and M. P. A. Viegers, "EXAFS and Near Edge Structures III," K. O. Hodgson, B. Hedman, and J. E. Penner-Hahn, Editors, p. 517, Springer-Verlag, Berlin (1984).
21. F. W. H. Kampers, F. B. M. Duivenvoorden, J. B. A. D. van Zon, P. Brinkgreve, M. P. A. Viegers, and D. C. Koningsberger, *Solid State Ionics*, **16,** 55 (1985).
22. R. Guan, H. Hashimoto, and T. Yoshida, *Acta Cryst.*, **B40,** 109 (1984).
23. R. Guan, H. Hashimoto, K. H. Huo, and T. Yoshida, *ibid.*, **B43,** 343 (1987).
24. P. Pichat, J.-M. Hermann, J. Disdier, H. Courbon, and M.-N. Mozzanega, *Nouv. J. Chim.*, **5,** 627 (1981).
25. J. B. A. D. van Zon, D. C. Koningsberger, H. F. J. van't Blik, and D. E. Sayers, *J. Chem. Phys.*, **82,** 5742 (1985).
26. R. W. G. Wyckoff, "Crystal Structures," 2nd ed., John Wiley & Sons, New York (1963).
27. T. I. Morrison, G. K. Shenoy, and D. Niarchos, *J. Appl. Cryst.*, **15,** 388 (1982).
28. M. Sano, T. Maruo, and H. Yamatera, *Bull. Chem. Soc. Jpn.*, **56,** 3287 (1983).
29. R. B. Greegor and F. W. Lytle, *J. Catal.*, **63,** 476 (1980).
30. M. D. Ward, J. R. White, and A. J. Bard, *J. Am. Chem. Soc.*, **105,** 27 (1983).
31. J. S. Curran and D. Lamouche, *J. Phys. Chem.*, **87,** 5405 (1983).
32. W. J. Albery and P. N. Bartlett, *This Journal*, **131,** 315 (1984).
33. P. Bindra and J. Roldan, *J. Appl. Electrochem.*, **17,** 1254 (1987).
34. M. Paunovic, *This Journal*, **124,** 349 (1977).
35. A. Vaskelis and A. Jagminiené, *Surf Coat. Technol.*, **27,** 301 (1986).
36. L. Meites, *J. Am. Chem. Soc.*, **71,** 3269 (1949).
37. M . Pourbaix, "Atlas of Electrochemical Equilibria in Aqueous Solutions," 2nd English Edition, p. 387, National Association of Corrosion Engineers, Texas (1974).
38. H.-D. Speckmann, M. M. Lohrengel, J. W. Schultze, and H.-H. Strehblow, *Ber. Bunsenges. Phys. Chem.*, **89,** 392 (1985).
39. H.-H. Strehblow and B. Titze, *Electrochim. Acta*, **25,** 839 (1980).
40. R. L. Deutscher and R. Woods, *J. Appl. Electrochem.*, **16,** 413 (1986).
41. U. Collisi and H.-H. Strehblow, *J. Electroanal. Chem.*, **210,** 213 (1987).
42. E. C. Dutoit, F. Gardon, and W. P. Gomes, *Ber. Bunsenges. Phys. Chem.*, **80,** 1285 (1976).
43. M. V. Rao, K. Rajeshwar, V. R. Pal Verneker, and J. Dubow, *J. Phys. Chem.*, **84,** 1987 (1980).
44. A. E. Rakhshani, A. A. Al-Jassar, and J. Varghese, *Thin Solid Films*, **148,** 191 (1987).
45. A. E. Rakhshani and J. Varghese, *ibid.*, **157,** 87 (1988).
46. Y. Nakato and H. Tsubomura, *J. Photochem.*, **29,** 257 (1985).
47. Y. Nakato, K. Ueda, H. Yano, and H. Tsubomura, *J. Phys. Chem.*, **92,** 2316 (1988).
48. J. S. Curran, J. Domenech, N. Jaffrezic-Renault, and R. Philippe, *ibid.*, **89,** 957 (1985).
49. P. Bindra and J. Roldan, *This Journal*, **132,** 2581 (1985).
50. K. Balakrishnan and V. K. Venkatesan, *Electrochim. Acta*, **24,** 131 (1979).